Flow Separation behind an Axisymmetric After-body and Impact of Grooves at Trailing Edge

Xinhui Lu[1], Huanxin Lai [1]
[1]School of Mechanical and Power Engineering,
East China University of Science and Technology,
130 Meilong Road, Xuhui District, Shanghai, P. R. China
826219871@qq.com; hlai@ecust.edu.cn

Abstract - In this paper, Embedded Large Eddy Simulation (ELES) is used to study the separated flow behind an axisymmetric after-body of rocket. The impacts of grooves added to the end of main body for passive load control are discussed. Three cases include the original after-body without groove (Prototype), with 6 grooves in azimuthal direction (Groove6), and with 12 grooves (Groove12) are compared and analysed. The pressure fluctuation on the after-body wall are analysed by using the Proper Orthogonal Decomposition (POD) method. The results show that the added grooves at the trailing edge can promote the flow mixing in the shear layer, so that the size of the separated flow zone with high pressure fluctuation is reduced in the flow direction, which is beneficial to improve the stability of the afterbody. The POD analysis is focused on the anti-symmetric mode (m=1) which characterizes the azimuthal instability. The results show that the energy proportion of the single helical mode (m=1) decreases in Groove6 and Groove12 cases, and the decrease is relatively significant in Groove6 case. This mode is an antisymmetric mode, and reducing its energy proportion is beneficial to improve stability.

Keywords: axisymmetric after-body, flow separation, embedded large eddy simulation, proper orthogonal decomposition

1. Introduction

The transition from the end of the rocket to the nozzle has a geometric structure that resembles a backward-facing step (BFS) configuration often referred to as the axisymmetric after-body. The flow separation caused by this structure will increase resistance and cause flutter and buffeting, which is not conducive to high-speed flight [1]. Therefore, the unsteady mechanism of the flow separation behind the axisymmetric after-body and its effective control are the basic problems of rocket flight stability.

Many scholars have studied the flow separation behind the axisymmetric after-body through experiment and simulation methods and have obtained some basic understanding. In experiment aspect, Depres et al. [2] studied the impact of jets and boosters on flow separation behind the axisymmetric after-body through wind tunnel experiment. Some advanced instruments and materials such as high-frequency oscillating hot wire (OHW) sensors [3] and platinumporphyrin complexes (PtTFPP) [4] are also used to study the pressure dynamics on the axisymmetric after-body. In order to explore an effective control method for the separated flow behind the axisymmetric after-body, Scharnowski et al. [5] used Particle Image Velocimetry (PIV) technology to study the effect of adding control loops at the trailing edge of the after-body. It was shown that the rectangular and circular control loops are beneficial to enhance the mixing of the shear layer and can reduce the reattachment length and the pressure fluctuation. In simulation aspect, Deck et al. [6] reproduced the tunnel experiment of Depres et al. [2] by simulation, and later generations did further research on this basis. Weiss et al. [7] added jets in the shear layer or in the recirculation area of the separated flow, and the results showed that the jets in the recirculation area directly acts on the coherent structure of the flow field, which can better reduce the side load. To elucidate the three-dimensional organization of the fluctuating pressure field related to each of the characteristic frequencies behind the axisymmetric after-body, a dynamic mode (DMD) analysis has been performed [8]. These studies provide strong support for the understanding and control of the separated flow behind the axisymmetric after-body, but the unsteady mechanism is still unclear and the control methods are less understood. For example, Scharnowski et al. [5] added control loops at the trailing edge of the after-body, although the pressure fluctuation was reduced, but they did not further analyze the asymmetry caused by the control

loops in the azimuthal direction. The asymmetric force in the azimuthal direction may destabilize the rocket, which is a significant basis for evaluating the quality of the flow control method.

This paper takes the geometric structure of Ariane 5 as the prototype and uses Embedded Large Eddy Simulation (ELES) to study the separated flow behind the axisymmetric after-body. The impacts of grooves added to the end of main body for passive load control are discussed, and the pressure fluctuation on the after-body wall are analysed by using the Proper Orthogonal Decomposition (POD) method. It provides a basis for further understanding of the separated flow.

2. Numerical Objects and Models
2.1. Cases for Study
The prototype of axisymmetric after-body in this paper is from the reference [8]. The Reynolds number of the original flow field ($Re_D = 1.2\times10^6$) is high, and it is located in the second auto simulation region, and the flow has similar properties, so this paper uses 1:10 scale models for research.
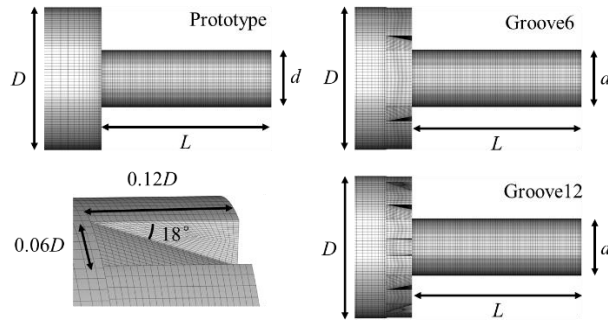

Fig. 1: Geometric model of axisymmetric after-body.

In order to consider the impacts of grooves added to the end of main body for passive load control, 6 grooves (Groove6) and 12 grooves (Groove12) are evenly arranged at trailing edge with a depth of 0.06D, a width of 0.12D, and an inclination of 18 deg (as shown in Fig. 1). The diameter of the large cylinder is reduced from $D = 100$ mm to $D =10$ mm, and the characteristic aspect ratios are $L/D = 1.2$ and $d/D = 0.4$, with L being the length of the small cylinder and d being the diameter of the small cylinder.

2.2. Numerical Methodology
Large Eddy Simulation (LES) has very high requirements on grids at the wall boundary layer when the Reynolds number are high, and the global large eddy simulation will consume a significant amount of computing resources. Therefore, the computational domain is partitioned in this paper. The incoming flow area is simulated by the Reynolds-averaged equations (RANS) method, the flow separation area is simulated by the Large Eddy Simulation (LES) method, and the velocity fluctuation algorithm is set at the interface between RANS and LES. This approach is often referred to as Embedded Large Eddy Simulation (ELES).

The standard $k-\varepsilon$ model is used in the RANS area, and the Wall-Adapting Local Eddy-Viscosity (WALE) model is used in the LES area. In the WALE model, the eddy viscosity is modeled by：

$$\mu_t = \rho L_s^2 \frac{(S_{ij}^{d'} S_{ij}^{d'})^{3/2}}{(\overline{S}_{ij}\overline{S}_{ij})^{5/2} + (S_{ij}^{d'} S_{ij}^{d'})^{5/4}} \tag{1}$$

$$L_s = \min(\kappa d', C_w V^{1/3}) \tag{2}$$

$$S_{ij}^{d'} = \frac{1}{2}(\bar{g}_{ij}^2 + \bar{g}_{ji}^2) - \frac{1}{3}\delta_{ij}\bar{g}_{kk}^2 \qquad (3)$$

$$\bar{g}_{ij} = \frac{\partial \bar{u}_i}{\partial x_j} \qquad (4)$$

where κ is the von Kármán constant, $C_\mu = 0.09$, $C_w = 0.325$, d' is the distance to the closest wall, V is the volume of the computational cell and $\bar{u}_i$ is the mean velocity components.

2.3. Computational Domain and Boundary Conditions

As shown in Fig. 2, the size of the computational domain is $28D$ in the flow direction and $10D$ in the radial direction. $-14 \le x/D \le 0$ is the RANS area, $0 \le x/D \le 14$ is the LES area, and the separation point is at $x/D = 0$. The number of grid cells for three cases are 4.24 million (Prototype), 4.50 million (Groove6) and 4.64 million (Groove12). Cylinder part adopts O-type mesh division, and the grooves use Y-type mesh division. To ensure $y^+ < 5$, the thickness of the first layer of grids on the wall is 10^{-4} m.
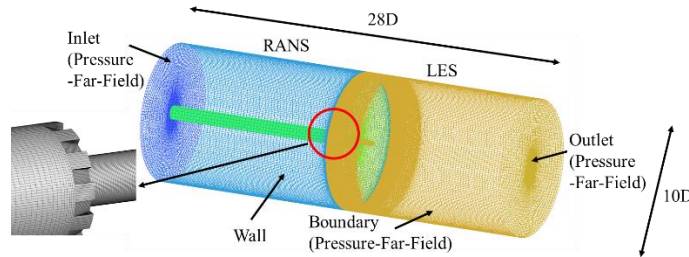

Fig. 2: Computational domain and grid.

For the boundary conditions, set the inlet, outlet and surrounding as pressure far-field boundary conditions, and the axisymmetric after-body wall is a non-slip adiabatic condition. This study focuses on high subsonic flow regime with Mach number M = 0.7 and static pressure $P_s = 7.2 \times 10^4$ Pa. The fluid medium is set as ideal gas, and its viscosity is the Sutherland model. The transient time step is 1.2×10^{-6} s. Spatial and time discretization is based on second-order upwind and second-order implicit form. After the fluid has flowed through the computational domain 10 times ($280D$), the flow field is considered to be sufficiently developed, the sampling time is 1.2×10^{-2} s, and a total of 1200 samples are collected.

3. Analysis of Flow Features
3.1. Average Properties of Flow Separation

In order to verify the reliability of the calculation model, the mean wall pressure coefficient is compared with the experimental data.

$$C_p = \frac{p - p_\infty}{\frac{1}{2}\rho U_\infty^2} \qquad (5)$$

Where p, p_∞, ρ and U_∞ represent the pressure, the freestream pressure, the density and the freestream velocity, respectively. As shown in Fig. 3, the results of the numerical simulation are in good agreement with the experiments, but there are certain differences for $0 \le x/D \le 0.6$, reflecting the complexity of the flow in the recirculation region. Three different regions can be distinguished. First, C_p gradually decreases due to the influence of the recirculation area on the upstream

flow for $x/D \leq 0$. After the separation point ($x/D=0$), C_p further slowly decreases because the fluid velocity in the recirculation area increases for $0 \leq x/D \leq 0.6$. The high-speed fluid directly impacts the wall of the after-body, enormous pressure, and C_p increases rapidly for $0.6 \leq x/D \leq 1.2$. C_p at the center of the groove (valley) and non-groove (peak) were intercepted for analysis in Groove6 and Groove12 cases. Groove6_valley and Groove12_valley decreases rapidly at $x/D \approx -0.3$, which is caused by the reflow at the groove. Likewise, Groove6_peak and Groove12_peak slightly near the groove. Groove12 and Prototype cases are more similar, and the pressure recovery region in Groove6 case moves upstream, indicating that its reattachment point is more advanced.
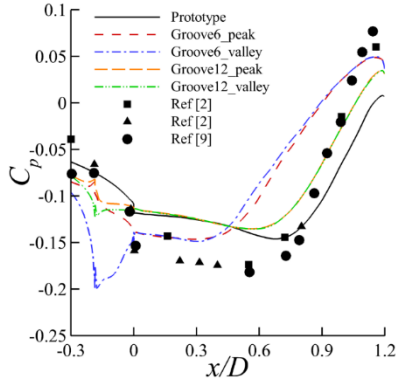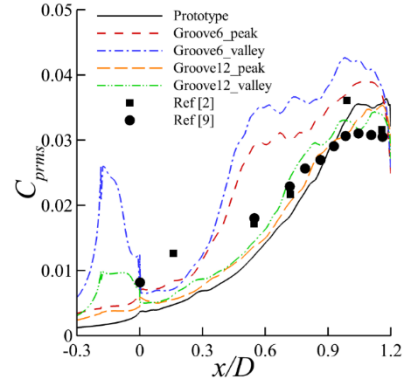

Fig. 3: Mean wall pressure coefficient.

Fig. 4: RMS pressure fluctuation coefficient.

The RMS wall pressure coefficient reflects the fluctuation level of the pressure, which is very important for the force balance of the after-body. It is defined as:

$$C_{prms} = \frac{\sqrt{p_1'^2 + p_2'^2 + ... + p_n'^2}}{\frac{1}{2}\rho U_\infty^2} \qquad (6)$$

Where p_i', ρ and U_∞ represent the pressure fluctuation, the density and the freestream velocity, respectively. The numerical simulation results in Fig. 4 have a certain gap with the experiment for $0 \leq x/D \leq 0.6$, but are in good agreement with the experiment at the end of the after-body, which corresponds to the mean wall pressure coefficient. C_{prms} has a steady increase in the range $0 \leq x/D \leq 0.9$ and a maximum $C_{prms} \approx 0.035$ is reached close to the mean reattachment point. This phenomenon is also observed in many separated flows, where Hudy et al. [10] believes that the increase of C_{prms} is likely due to the organized shear layer structures which get stronger and move closer to the wall. Reducing the wall pressure fluctuation is very important for the stability of the after-body. Groove6_valley and Groove12_valley generate larger pressure fluctuations at $x/D \approx -0.3$, and the grooves will cause higher pressure fluctuation at the front of the after-body, but drop faster at the trailing edge of the after-body. The moment at the trailing edge of the after body is larger, which has a more important impact on the stability.

It can be seen from the above analysis that Groove6 case has better control effect than Groove12, indicating that the number of grooves has a certain influence on the separated flow field. Fig. 5 is the streamline diagram of the after-body separation region ($\theta = 0°$). In Prototype case, after the incoming flow passes through the separation point, the boundary layer and the wall are separated, and shear flow is formed with the external fluid in the separation region. The separated shear layer is reattached downstream, forming a recirculation area within the reattachment point, and secondary separation occurs after the fluid leaves the after-body, forming a secondary recirculation area. In Groove6

case, the grooves make the fluid reattach to the wall earlier, while the reattachment point in Groove12 case is not as advanced as that of Groove6 case. In Groove12 case, the corner vortex flows back to the grooves, weakening the control effect of the grooves, which is consistent with the mean wall pressure coefficient and RMS wall pressure coefficient.
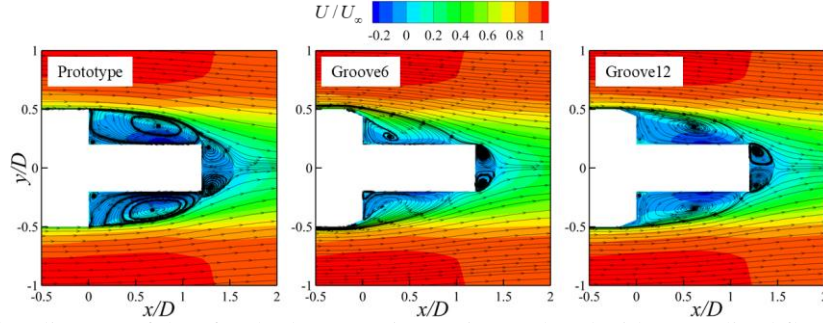

Fig. 5: Streamline diagram of the after-body separation region (colored with normalized flow velocity).
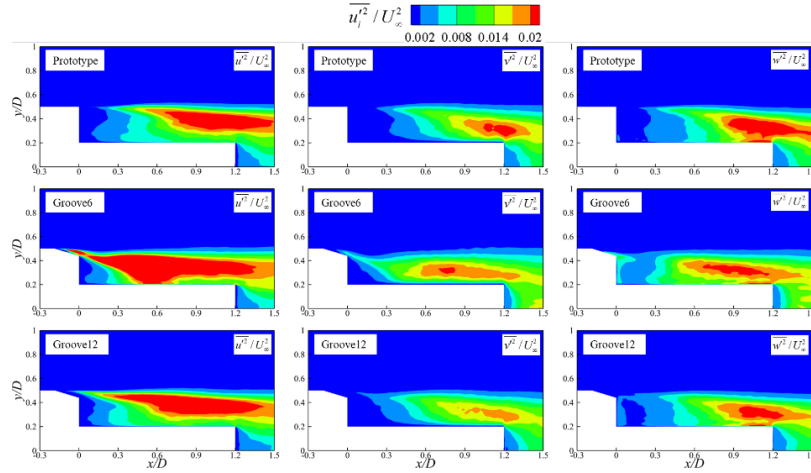

Fig. 6: Velocity fluctuation in the separation zone.

The separated shear layers cause strong velocity fluctuation. As shown in Fig. 6, there is a severe velocity fluctuation near the mean reattachment. The spatial distribution of velocity fluctuation in the three directions is similar, and the radial velocity component $\overline{w'^2}$ is larger than the circumferential velocity component $\overline{v'^2}$. In Groove6 and Groove12 cases, due to the advance of the reattachment, there is a higher velocity fluctuation in the front half of the after-body, but the velocity fluctuation in the downstream is weakened. Therefore, the grooves can enhance the mixing of the fluid, so that the region with higher velocity fluctuation is compressed in the flow direction, which is beneficial to improve the stability.

In order to analyze the control effect of the groove in the azimuthal direction, a spanwise plane at $x/D=1.1$ was investigated. This plane is in the recirculation area for the Prototype case, while for the Groove6 and Groove12 cases the shear layer has been reattached. As shown in Fig. 7 (a), the main feature is reverse flow in Prototype case and the shear layer forms a circumferential periodic shape in Groove6 case, but there is still a small amount of reverse flow in Groove12 case.

Fig. 7 (b) is the Turbulent Kinetic Energy (*TKE*) of the plane, which is defined as:

$$TKE = \frac{1}{2}(\overline{u'^2} + \overline{v'^2} + \overline{w'^2}) \tag{7}$$

Where $\overline{u'^2}$, $\overline{v'^2}$ and $\overline{w'^2}$ represent the mean velocity fluctuation component. *TKE* shows that there is a strong velocity fluctuation in the shear layer. The distribution of *TKE* at the plane of the three cases is relatively close, and they all show periodic changes in the azimuthal direction. The azimuthally concave area is the location of the grooves, while increasing grooves did not change the value of *TKE* significantly.
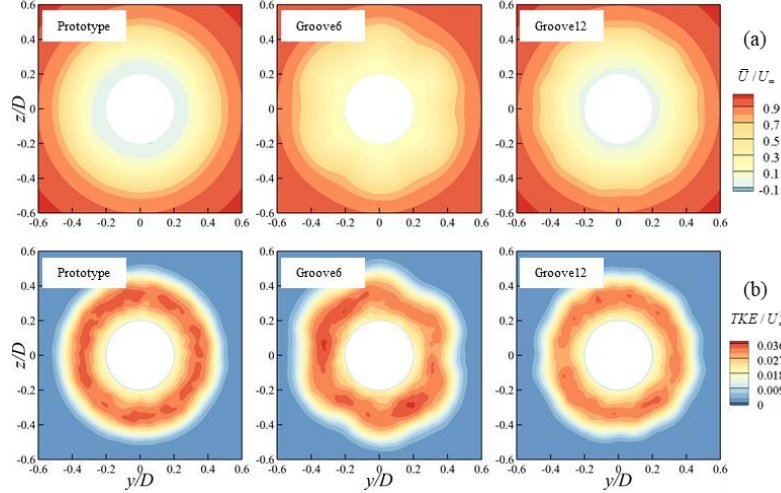

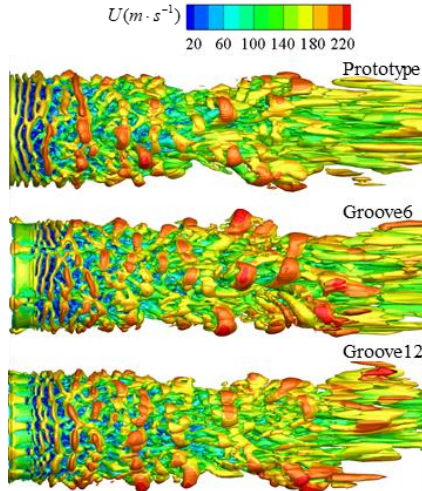Fig. 7: Flow velocity and turbulent kinetic energy ($x/D = 1.1$).

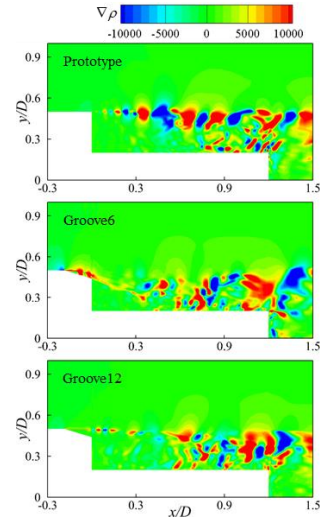Fig. 8: Iso-surfaces of Q-criteria ($Q = 50U_\infty^2 / D^2$).

Fig. 9: Density gradients.

3.2. Transient Vortex Structure

The stability of the axisymmetric after-body is closely related to the development of the vortex at the separation zone, and the Q criterion is used to identify and visualize the vortex.

$$Q = \frac{1}{2}(\Omega_{ij}\Omega_{ij} - S_{ij}S_{ij}) \tag{8}$$

Where Ω_{ij} and S_{ij} represent the symmetric and antisymmetric parts of the velocity gradient, respectively. By adjusting the threshold to observe the turbulent structures, Fig. 8 shows the details of the flow field displayed by the

iso-surface of $Q = 50U_\infty^2 / D^2$. In Prototype case, the after-body separation area first rolls up toroidal eddies, which are closely related to the K-H instability, and they will rapidly replaced by large three-dimensional structures. After the break up of the eddies the main structures appear to be longitudinal eddies, which is consistent with the result that $\overline{w'^2}$ is larger than $\overline{v'^2}$ in Fig. 6. At the same time, hairpin eddies can be observed near the reattachment.

The fluid density gradient $\nabla\rho$ in Fig. 9 corresponds to the Q criterion. In Prototype case, the strength of $\nabla\rho$ at the separation point is larger, reflecting strong K-H instability, and there will also be a larger density gradient region near the reattachment. In Groove6 case, a large density gradient will be generated at the grooves, and due to the advance of the reattachment point, the larger density gradient region will also advance accordingly. The Groove12 case is similar to the Prototype case, and the control effect is not obvious, which is consistent with the previous analysis.

4. POD Analysis for Pressure Field

Proper Orthogonal Decomposition (POD) can characterize the energy-containing structure in the flow field according to the fluctuation intensity, and is widely used to analyze the spatial structure and time evolution process of the flow field. POD method defines the eigenvectors of the covariance matrix of the flow field samples as spatial modes, and the corresponding eigenvalues represent the intensity of modes. In this paper, the instantaneous pressure fluctuation p' on the after-body wall is extracted to decompose.

$$p'(x,\theta,t) = \sum_{m=-N_\theta/2}^{N_\theta/2} p'^m(x,t)e^{im\theta} \tag{9}$$

$$M(x,t) = \sum_{j=1}^{N_t} a_j(t)\phi_j(x) \tag{10}$$

$$M(x,t) = \underset{S_p \times R}{\Phi^m} \underset{R \times R}{\Sigma^m} \underset{R \times N_t}{(\Psi^m)^T}$$

$$\begin{cases} \Phi^m = [\phi_1,...,\phi_N] \\ \Sigma^m = \text{dig}[\sigma_1,...,\sigma_N] \\ \Psi^m = [\psi_1,...,\psi_N] \end{cases} \tag{11}$$

In Eqs. (9) – (11), $e^{im\theta}$ is the basis function, $M(x,t)$ is the sample matrix obtained from the circumferential mode $p'^m(x,t)$, S_p is the number of grid nodes, N_t is the number of samples, and $R = \min(S_p,N_t)$ is the number of diagonal elements of the singular value matrix. According to the characteristics of singular value decomposition (SVD), ϕ_j in Φ^m is the jth POD mode, and $\sigma_j^2 / N_t = \lambda_j$, Ψ^m is the time coefficient matrix.
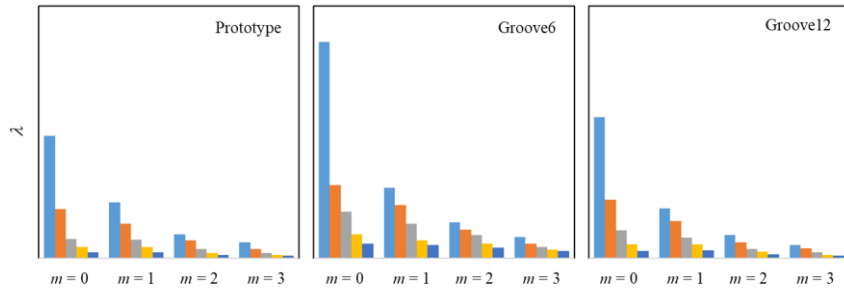

Fig. 10: Eigenvalues under different azimuthal modes.

Fig. 10 shows the first 5 eigenvalues in circumferential mode (m=0-3). These eigenvalues represent the variance of physical quantities. The larger the eigenvalue, the greater the disturbance, that is, the greater the energy. In the three the first eigenvalues of m=0 and m=1 are larger, indicating that the breathing mode (m=0) and the single helical mode have higher energy, which can characterize the main pressure properties of the after-body wall. In Groove6 cases, the eigenvalue of the breathing mode (m=0) increases significantly, and the proportion of the eigenvalues of the single helical mode (m=1) decreases, but it is only slightly improved in Groove12 case, which is consistent with the previous flow field analysis.

5. Conclusion

The conclusions are as following:

(1) The separated flow behind the axisymmetric after-body has a large fluctuation level near the separation point and the mean reattachment point, which reflects the strong K-H instability.

(2) In Groove6 case, size of the separation bubble is reduced notably, indicating that the addition of grooves on the after-body can increase the mixing of the shear layer, so that the high fluctuation region of the separation zone is compressed in the flow direction.

(3) Breathing mode (m=0), single helical mode (m=1) and double helical mode (m=2) were decomposed by POD on the pressure fluctuation of the after-body wall. The energy proportion of the single helical mode (m=1) decreases in Groove6 and Groove12 cases, and the decrease is relatively significant in Groove6 case. This mode is an antisymmetric mode, and reducing its energy proportion is beneficial to improve stability.

Acknowledgements

References

[1] R. Pain, P. E. Weiss, and S. Deck, "Zonal Detached Eddy Simulation of the Flow Around a Simplified Launcher Afterbody," *AIAA. J*., vol. 52, no. 9, pp. 1967-1979, 2014.

[2] D. Depres, P. Reijasse, and J. P. Dussauge, "Analysis of Unsteadiness in Afterbody Transonic Flows," *AIAA. J*., vol. 42, no. 12, pp. 2541-2550, 2004.

[3] Y. Li, A. M. Naguib, and L. M. Hudy, "Two-Point Measurements of Wall Shear Stress Beneath an Axisymmetric Separating/Reattaching Flow," *AIAA. J*., vol. 46, no. 10, pp. 2649-2652, 2008.

[4] M. Bitter, T. Hara, R. Hain, D. Yorita, K. Asai, and C. Kahler, "Characterization of Pressure Dynamics in an Axisymmetric Separating/Reattaching Flow Using Fast-responding Pressure-sensitive Paint," *Exp. Fluids*., vol. 53, no. 6, pp. 1737-1749, 2012.

[5] S. Scharnowski, M. Bosyk, F. Schrijer, and B. W. Oudheusden, "Passive Flow Control for the Load Reduction of Transonic Launcher Afterbodies," *AIAA. J*., vol. 57, no. 5, 2019.

[6] S. Deck, and P. Thorigny, "Unsteadiness of an Axisymmetric Separating-Reattaching Flow: Numerical Investigation," *Phys. Fluids*., vol. 19, no. 6, 065103, 2007.

[7] P. E. Weiss, and S. Deck, "Control of the Antisymmetric Mode (m=1) for High Reynolds Axisymmetric Turbulent Separating/Reattaching Flows," *Phys. Fluids*., vol. 23, no. 9, pp. 113-147, 2011.

[8] R. Pain, P. E. Weiss, S. Deck, and J. C. Robinet, "Large Scale Dynamics of a High Reynolds Number Axisymmetric Separating/Reattaching Flow," *Phys. Fluids*., vol. 31, no. 12, 125119, 2019.

[9] P. Meliga, and P. Reijasse, "Unsteady Transonic Flow behind an Axisymmetric Afterbody Equipped with Two Boosters," in *Proceedings of the 25th AIAA Applied Aerodynamics Conference (AIAA)*, Miami, FL, 2007, Paper No. 4564.

[10] L. M. Hudy, A. M. Naguib, and W. M. Humphreys, "Wall-pressure-array Measurements Beneath a Separating/Reattaching Flow Region," *Phys. Fluids*., vol. 15, no. 3, pp. 706-717, 2003.